# Fine Tuning of the Relaxometry of γ-$Fe_2O_3$@$SiO_2$ Nanoparticles by Tweaking the Silica Coating Thickness

**Sonia L. C. Pinho,[†,‡] Giovannia A. Pereira,[‡,⊥] Pierre Voisin, Jinane Kassem,[§] Véronique Bouchaud,[§] Laetitia Etienne,[†] Joop A. Peters,[¶] Luis Carlos,[‡] Stéphane Mornet,[†] Carlos F. G. C. Geraldes,[⊥,*] João Rocha,[‡,*] and Marie-Hélène Delville[†,*]**

[†]CNRS, Université de Bordeaux, ICMCB, 87 avenue du Dr. A. Schweitzer, Pessac, F-33608, France, [‡]Departments of Chemistry and Physics, CICECO, University of Aveiro, 3810-193 Aveiro, Portugal, [§]Centre de Résonance Magnétique des Systèmes Biologiques, UMR 5536 CNRS, UMR 5536 CNRS, 146 rue Victor Segalen, F-33076 Bordeaux cedex, France, [⊥]Department of Life Sciences, Faculty of Science and Technology, and Centre of Neurosciences and Cell Biology, University of Coimbra, 3001-401 Coimbra, Portugal, and [¶]Laboratory of Biocatalysis and Organic Chemistry, Department of Biotechnology, Delft University of Technology, Julianalaan 136, 2628 BL Delft, The Netherlands

**ABSTRACT** We report the fine-tuning of the relaxometry of γ-$Fe_2O_3$@$SiO_2$ core−shell nanoparticles by adjusting the thickness of the coated silica layer. It is clear that the coating thickness of γ$Fe_2O_3$@$SiO_2$ nanoparticles has a significant impact on the $r_1$ (at low $B_0$ fields), $r_2$, and $r_2^*$ relaxivities of their aqueous suspensions. These studies clearly indicate that the silica layer is heterogeneous and has regions that are porous to water and others that are not. It is also shown, that the viability and the mitochondrial dehydrogenase expression of the microglial cells do not appear to be sensitive to the vesicular load with these core−shell nanoparticles. The adequate silica shell thickness can therefore be tuned to allow for both a sufficiently high response as contrast agent, and adequate grafting of targeted biomolecules.

**KEYWORDS:** iron oxide nanoparticles · silica coating · NMR relaxation rates · MRI contrast agents

Nanoparticles (NPs) made of inorganic or organic materials exhibit many novel properties compared with the bulk materials.[1] Magnetic NPs have unique properties such as superparamagnetism, high coercivity, low Curie temperature, and high magnetic susceptibility, *etc*.[2] Magnetic NPs are of great interest for a broad range of applications, from magnetic fluids to data storage, catalysis,[3] and bioapplications.[4] Examples of applications of NPs in the study of biology and biomedicine are magnetic bioseparation,[5] cell sorting,[6,7] detection of biological entities,[8] clinical diagnosis, and therapy (such as MRI, magnetic resonance imaging),[9−18] MFH (magnetic fluid hyperthermia),[19] targeted drug delivery,[20−23] immunoassays,[24] and biomacromolecules purification.[25] Magnetic iron oxide NPs play an important role in these applications, and they have been used in *in vitro* diagnosis for about 50 years.[26] In the past decade, numerous investigations have been carried out in the field of magnetic NPs,[27] especially on magnetite and maghemite, owing to their biocompatibility, FDA approval,[28] and absence of toxicity.[29−31]

The control of the nanoparticles size, shape, stability, and dispersibility in specific solvents is a technological challenge. Bioapplications, for example, require water-solubility and colloidal stability. However, most reported synthesis routes for high-quality nanoparticles of metals,[32,33] semiconductors,[34,35] and metal oxides[36−38] involve nonaqueous solvents and coating with monolayers of hydrophobic surfactants. Several strategies to tackle these challenges have been formulated,[39] such as (i) polymer coating,[40,41] (ii) exchanging the original hydrophobic stabilizer with dendrons,[42,43] thiols, or even oligomeric phosphines,[44] and (iii) silica coatings.[45−53]

To expand the scope of the iron oxide NPs in biological applications, biomolecules have been employed as coatings, such as amino acids,[54] vitamins,[55,56] proteins,[57] antibodies,[58,59] polypeptides,[60] biotin, avidin,[61] and saccharides.[62] However, silica coating remains one of the most popular and well-known techniques for nanoparticle surface modification, because the resulting cross-linked silica shell protects the core from the environment and *vice versa*. The silica coating also provides colloidal stability in biological solutions by avoiding interparticle interactions and agglomeration. Furthermore, it can act as an anchor for the binding of biological vectors at the NPs surface.[63] While there are numerous

*Address correspondence to delville@icmcb-bordeaux.cnrs.fr.

Received for review May 21, 2010 and accepted August 04, 2010.

**Published online August 26, 2010.** 10.1021/nn101129r

publications concerning silica coatings, only a few methods have been reported for the preparation of water-soluble silica-coated nanoparticles with a high colloidal stability and with sizes below 20 nm.[45,50,53]

Particles with tunable size are important when considering biomedical applications. While small nanoparticles exhibit reduced nonspecific interactions, minimal steric effects, and high clearance rates,[64] larger nanoparticles are subjected to internalization by macrophages. The thickness of the silica shell has also a strong influence on the physical properties of the NPs, especially in terms of contrast agent efficacy for magnetic resonance imaging. In this paper, we describe the synthesis of $\gamma$-$Fe_2O_3$@$SiO_2$, core−shell nanoparticles with tuned shell thicknesses. These particles were characterized by transmission electron microscopy (TEM), zeta potential determinations, diffuse reflectance infrared Fourier-transform (DRIFT), and nuclear magnetic resonance (NMR). The longitudinal ($T_1$) and transversal ($T_2$) relaxation times of aqueous suspensions of the prepared particles were measured, and their cytotoxicity was investigated. We show that the shell thickness of $\gamma$-$Fe_2O_3$@$SiO_2$ nanoparticles has a significant impact on their relaxivities. This silica layer exhibits two regions around the core, one, which is porous to water, and a second one, which is not.

## RESULTS AND DISCUSSION

The aqueous maghemite suspension was synthesized by basic precipitation from iron chlorides, followed by complete oxidation of the magnetite material. For the coating, a polymerization of silane monomers in the presence of the nanoparticles under Stöber conditions[65,80] was performed. This procedure is widely used since it provides uniform silica coating with a controllable thickness. Stöber's conditions involve alcohol−water−ammonia as the medium and tetraethoxysilane (TEOS) as the silane monomer (Supporting Information, Figure S5). A preactivation of the surface of the nanoparticles through acidic treatment was found to improve the silica coating, leading to a simple and highly reproducible method for producing monodispersed water-soluble stable colloidal nanoparticles with silica shells whose thickness is tunable in the range 2−70 nm.

To tune the silica shell thickness, the required amount of TEOS was calculated from the initial and the desired final particle size,[66,67] taking into account the number of $\gamma$-$Fe_2O_3$ nanoparticles, $N_{part}$, using eq 7 in the experimental section. The estimated and experimental thicknesses of the silica coatings are summarized in Table 1, while Figure 1 displays the TEM images obtained at various stages of the NPs synthesis.

The TEM showed that spherical core−shell ($\gamma$-$Fe_2O_3$@$SiO_2$) nanoparticles with different shell sizes were obtained; as clearly evidenced by these images, all the $\gamma$-$Fe_2O_3$ particles were surrounded by the silica layer. The scheme on the right of the lower row of the images defines the measured size or diameter ($d$) of the NPs, and their silica shell thickness ($t$). The average thickness of silica shells was determined from these images by measurements in four directions for each particle and at least 100 particles per $\gamma$-$Fe_2O_3$@$SiO_2$ sample, showing that the size dispersion of the particles is very small.

**TABLE 1. Synthesis of Maghemite Core−Shell ($\gamma$-$Fe_2O_3$@$SiO_2$) Nanoparticle: Comparison between Estimated and Experimental Values of Shell Thicknesses**

| sample | estimated shell thickness (nm) | experimental shell thickness (nm) | experimental diameter (nm) |
|---|---|---|---|
| 0A | 1 ± 1 | 2 ± 1 | 14 ± 2 |
| 1A | 4 ± 1 | 8 ± 2 | 27 ± 5 |
| 2A | 10 ± 1 | 15 ± 4 | 40 ± 8 |
| 3A | 18 ± 2 | 20 ± 4 | 50 ± 7 |
| 4A | 23 ± 3 | 28 ± 4 | 66 ± 8 |
| 5A | 31 ± 3 | 52 ± 6 | 114 ± 14 |
| 6A | 56 ± 6 | 67 ± 5 | 145 ± 10 |

[a] Estimated shell thickness calculated with eq 7.

Figure 2 shows the relationship between the obtained shell thicknesses and the expected ones through calculations. They are proportional to the amount of TEOS added during the preparation. Note the deviation from a slope of 1, which is significant of the errors taking place at each step as well as some aggregation of the maghemite particles, as can be detected by TEM.

Figure 3 shows the zeta potential titrations as a function of pH, and both the pH range of stability and the isoelectric points (IEP) of the two types of particles (2.3 for silica and 7.0 for $\gamma$-$Fe_2O_3$). Silica has long been used as a nonmagnetic coating material in order to avoid aggregation or sedimentation of ferrofluid magnetic nanoparticles because of its extraordinary stability over a wide range of polar and nonpolar solvents.

In particular, aqueous dispersions of silica are known to be stable over a large pH range (IEP at pH 2). The shift of the IEP toward lower pH values (from ~6.5−7 to ~2.5) upon coating (Figure 3) provides an additional confirmation that the coating was successful. The large negative zeta potential (−80 mV) at physiological pH of the coated NPs suggests that the aqueous suspensions will by highly stable under *in vivo* conditions and will not flocculate at pH 7.

DRIFT spectroscopy was also used to probe the effectiveness of the chemical coating of silica on the maghemite NPs (FF) (Supporting Information, Figure S6). Several absorption bands in the DRIFT spectrum of $\gamma$-$Fe_2O_3$@$SiO_2$ samples (Figure S6,c) are assigned to silica and clearly show that this material covers the surface of the maghemite NPs. The bound Si−OH groups are characterized by the very broad IR absorption band in the 2800−3700 $cm^{-1}$ region, whereas the so-called free Si−OH groups provide a narrow IR absorption

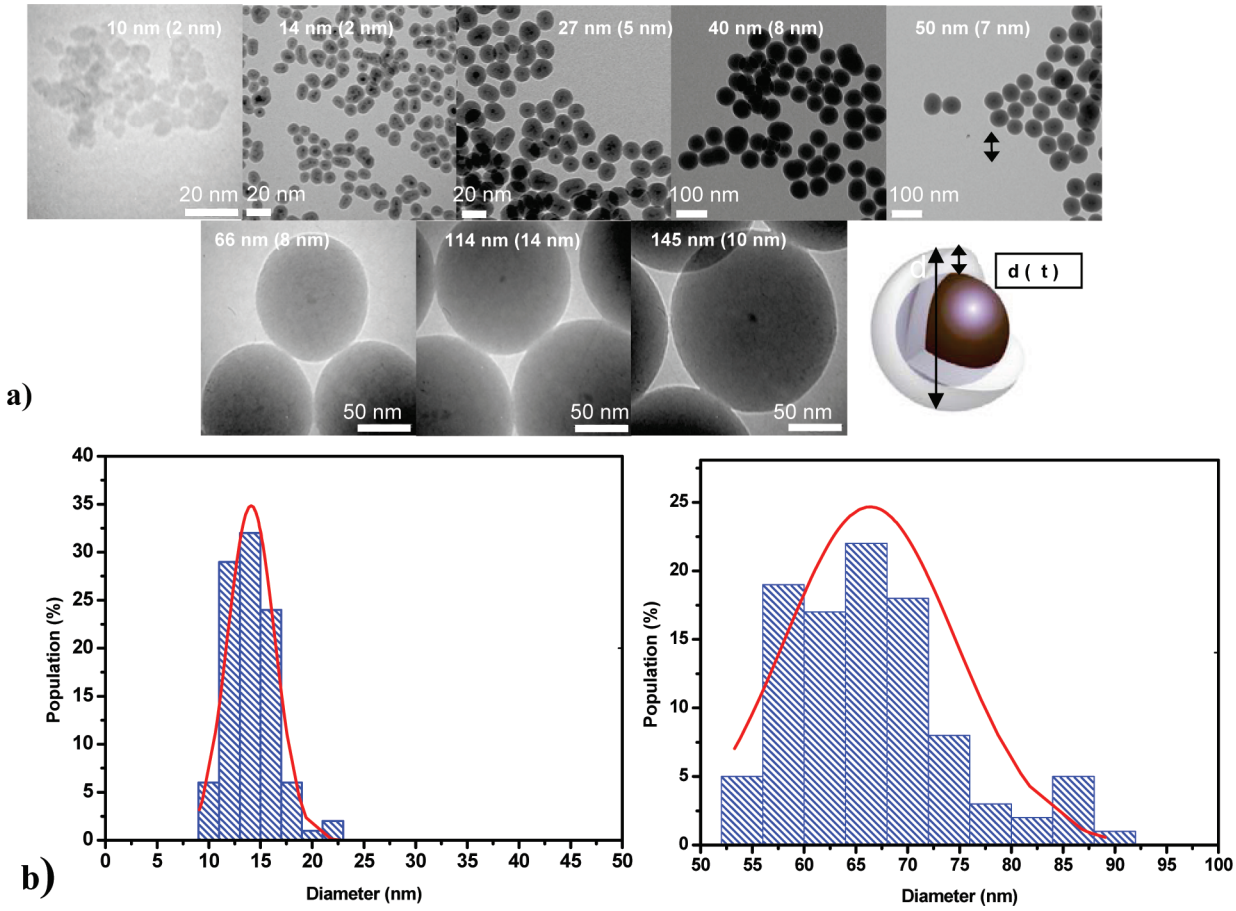


**Figure 1. (a) TEM images showing the average size (diameter *d*) of different maghemite core−shell ($\gamma$-$Fe_2O_3$@$SiO_2$) nanoparticles and of their silica shell thickness (*t*); (b) histograms with experimental size distributions of samples 0A ($\gamma$-$Fe_2O_3$@ $SiO_2$ 14 nm) (left) and 4A ($\gamma Fe_2O_3$@$SiO_2$ 28 nm) (right) and corresponding calculated normal cumulative distributions for the specified mean and standard deviation.**

band at 3630 $cm^{-1}$. The stretching band at 1635 $cm^{-1}$ shows the presence of residual physisorbed water molecules, while the large bands centered at 1864 $cm^{-1}$, 1108 $cm^{-1}$, and 796 $cm^{-1}$ are assigned to the Si−O and Si−O−Si stretching modes.

To investigate the influence of the shell thickness of the silica coating on the MRI contrast agent (CA) efficiency of the $\gamma$-$Fe_2O_3$ NPs, the $r_i$ ($i$ = 1, 2) relaxivities (defined as enhancement of $R_i = 1/T_i$, $i$ = 1, 2, the relaxation rates per mM concentration of CA) of the different core−shell NPs were measured at two resonance frequencies (20 and 500 MHz) and two temperatures (25 and 37 °C). Figure 4 shows typical values of the $r_1$ and $r_2$ relaxivities for the aqueous suspensions of $\gamma$-$Fe_2O_3$@$SiO_2$ NPs as a function of the diameter *d* of the NPs with a 10.0 nm diameter $\gamma$-$Fe_2O_3$ core and an increasing thickness of its silica layer, yielding *d* values of 14 nm (sample 0A) to 145 nm (sample 6A) (Table 2).

The $r_1$ values obtained at 20 MHz decrease with the increase of the silica shell thickness. This decrease is initially quite sharp, from 32.0 $s^{-1}$ $mM^{-1}$ for NPs without silica coating ($d$ = 10.0 nm) to 11.2 $s^{-1}$ $mM^{-1}$ for $d$ = 14 nm, while the $r_1$ values become very small (<2 $s^{-1}$ $mM^{-1}$) for $d$ > 25 nm (Figure 4, inset). At 500 MHz, $r_1$ values are very small in all cases, even in the absence of silica shell (Figure 4).

For superparamagnetic NPs, the relaxivities $r_i$ ($i$ = 1, 2) are dominated by the outer-sphere relaxation mechanism, which is due to the effect of local magnetic field gradients generated by the NPs on the water protons diffusing near their surface.[68,69] Taking into account the effect of water diffusion through the nonfluctuating magnetic field ($\mathbf{B}_0$), inhomogeneities created by the time-averaged value of the magnetic moment ($\langle\mu_z\rangle$) of the NPs aligned onto $\mathbf{B}_0$, and the effect of the fluctuation of the magnetic moment itself ($\Delta\mu_z$), a theoretical model was developed, where the $r_1$ and $r_2$ relaxivities contain terms proportional to $\langle\mu_z\rangle^2$, which define the Curie relaxation[70] and dominate at high fields, and fluctuating terms proportional to $\Delta\mu_z^2$ (Néel relaxation) that dominate at low fields.[69−71] This model accounts quite well for the magnetic field dependence of $r_1$ for ultrasmall particles of iron oxide (USPIO) (diameters of 10−40 nm) at high fields ($\mathbf{B}_0$ > 0.02 T, corresponding to ~0.8 MHz Larmor frequency), where Curie relaxation dominates, but does not account for the small $r_1$ dispersion observed at low fields (below 1 MHz), which depends on the crystal anisotropy energy.[72] Above 1 MHz,

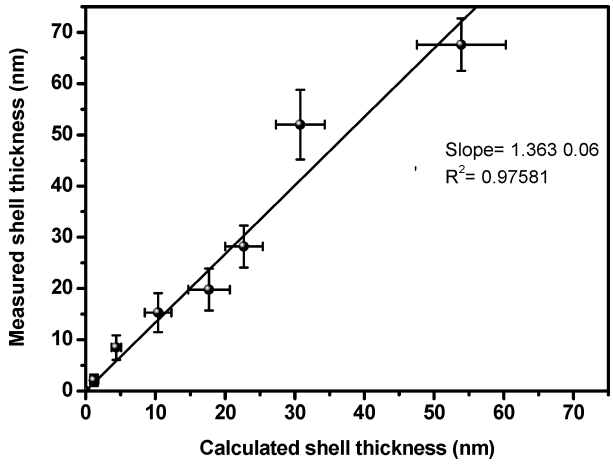


**Figure 2. Correlation between the experimental thickness of the silica shell as determined by TEM (*t*) and the thickness calculated with eq 7.**

$r_1$ depends on the translational diffusion correlation time $\tau_D$ and decreases with increase of the proton Larmor frequency $\omega_I$, with an inflection point defined by the condition $\omega_I \cdot \tau_D \approx 1$. $\tau_D = r_p^2/D$, where $D$ is the relative diffusion coefficient of the paramagnetic center and the water molecule and $r_p$ is the radius of the particle, which determines their distance of closest approach.

The decrease of the $r_1$ values at 20 MHz with the increase of the silica shell thickness reflects the decrease of the outer-sphere contribution of the core to $r_1$ due to the increase of the distance of closest approach of the diffusing bulk water molecules to the superparamagnetic core of the particle. This induces an increase of the translational diffusion correlation time, $\tau_D$. At least a large part of the silica layer is expected to be impermeable to water. The relative diffusion coefficient $D$ is expected to be nearly constant for all NPs. Being the sum of the diffusion constants of water ($D_{H_2O}$) and of the NP ($D_{NP}$); it is dominated by $D_{H_2O}$ because of the large size of the NPs and the slow diffusion of water in the putative silica surface layer. The very small $r_1$ values obtained at 500 MHz result from the expected field dependence of outer-sphere relaxation.

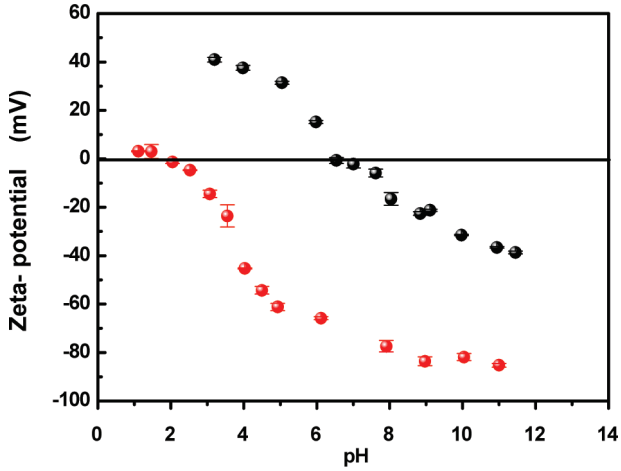


**Figure 3. Zeta potential titrations as a function of pH of γ-$Fe_2O_3$ (black) and γ-$Fe_2O_3$@$SiO_2$ (red) aqueous suspensions.**

The effective transverse relaxation rates ($R_2^*$) for the aqueous suspensions of the γ$Fe_2O_3$@$SiO_2$ NPs were obtained from the spectral line widths of their proton water resonance. Values of $R_{2p}^*$ (the paramagnetic contribution to $R_2^*$) were calculated by subtraction of the diamagnetic contribution of aqueous suspensions of diamagnetic iron oxide-free silica NPs from each paramagnetic contribution, using the spectral line widths for the various samples. The corresponding relaxivities, $r_2^*$, were also obtained (see Table 2). The line broadening effects reflect the dephasing of the water proton magnetic moments diffusing past the magnetic field gradients in the vicinity of the small superparamagnetic NPs, causing their $T_2$ shortening.

The transverse relaxation times are characterized by the correlation time parameters $\tau_D$, $(\Delta\omega)^{-1}$, and $\tau_{CP}$. The uncoated particles have a radius of 5 nm, from which it can be calculated that for these particles $\tau_D$ is $10^{-8}$ s. From simulations reported by Gillis *et al.*,[73] the transverse relaxivity may be predicted by the outer-sphere theory eq 1, where $\Delta\omega$ is the difference in the Larmor frequency at the particle surface and the infinity, and $v$ is the volume fraction of the particles.

$$r_2 = r_2^* = \frac{4}{9}\Delta\omega^2 v\tau_D \qquad (1)$$

Upon coating, both $\tau_D$ and $(\Delta\omega)^{-1}$ will decrease, and we assume that the outer-sphere regime remains valid.

The $r_2$ values were measured as a function of the time interval between two consecutive 180° pulses ($\tau_{CP}$) in a CPMG pulse sequence, for aqueous suspensions of the various NPs of increasing diameter. Figure S7 (see Supporting Information) shows that the transverse relaxivities of these NPs are virtually independent of $\tau_{CP}$ for all silica shell sizes. This observation is not surprising, since the $\tau_D$ values of the systems measured are all much smaller that the applied $\tau_{CP}$ values, and consequently the refocusing pulses are fully effective. Figure 4b and Table 2 show that the $r_2$ relaxivity (measured at $\tau_{CP} = 1.6$ ms) sharply decreases when the thickness of the coating of the NPs increases. As discussed above for $r_1$ effects, this results from the decrease of the outer-sphere contribution of the core to $r_2$ due to the increase of the distance of closest approach of the diffusing bulk water molecules to the superparamagnetic core of the particle.

Data show that $r_2 \cong r_2^*$ for the smallest particles (γ-$Fe_2O_3$ NPs (core), 0A and 1A), but $r_2 < r_2^*$ for particles with thicker coatings. It is possible that for the thicker coatings the silica layer is only impermeable to water up to a certain silica shell thickness. The diffusion of the water molecules in the permeable silica layer may be relatively slow. If in this layer the diffusion is so slow that the condition $\tau_D \gg (\Delta\omega)^{-1}$ holds, the diffusion correla-

tion time is not effective when refocusing pulses are applied and, consequently, the phase incoherence of the water protons is fully refocused in that part of the system, resulting in zero contribution to $r_2$. As far as $r_2$ and $r_2^*$ are concerned, it will be assumed that the particles consist of three spheres[74] with radii $r_c$, $r_i$, and $r_{diff}$ (Figure 5).

Here, $r_c$ is the radius of the core (5 nm), $r_i$ is the radius of the sphere around the core, that seems to be impermeable to water, and $r_{diff}$ is the radius of a sphere, in which any water molecule that is inside diffuses very slowly and does not contribute to $r_2$. Water molecules outside the latter sphere are assumed to contribute fully to $r_2$, whereas all water (including that inside the latter sphere) contributes to $r_2^*$.

Taking into account the distance dependence of $\Delta\omega$, $v$, and $\tau_D$, the following scaling may be applied:[75,76]

$$\Delta\omega_i = \Delta\omega_c\left(\frac{r_c}{r_i}\right)^3 \quad (2)$$

$$v_i = v_c\left(\frac{r_i}{r_c}\right)^3 \quad (3)$$

$$\tau_{D_i} = \tau_{D_c}\left(\frac{r_i}{r_c}\right)^2 \quad (4)$$

Combination of eqs (1−4) gives

$$r_2^* = r_{2,c}^*\left(\frac{r_c}{r_i}\right) \quad (5)$$

Similarly, it can be derived that

$$r_2 = r_{2,c}\left(\frac{r_c}{r_{diff}}\right) \quad (6)$$

Using the two latter equations and the experimental values of $r_2$ and $r_2^*$, the values of $r_i$ and $r_{diff}$ were calculated for the various samples (see Table 2 and Figure 5b). These calculated $r_{diff}$ values are in relatively fair agreement with the particle diameters obtained from the TEM measurements. The results also suggest that the water impermeable part of the silica coating tends to a maximum value of 40 nm, while the water permeable part increases with the coating thickness.

The cytotoxicity of the γ-$Fe_2O_3$@$SiO_2$ nanoparticles was assessed after incubations with microglial cell lines for $^3/_4$, 24, 48, 72, 96, 120, and 144 h. For each time point, cells were incubated or not with the nanoparticles (0.16 mM). Then, the cells were separated in two sets, one used as control and the other one being submitted to the MTT assay. This test was performed in order to characterize the viability of the cells and evaluate the residual toxicity after the internalization of the nanoparticles.[77] The cell viability tests (Figure 6), show that with and without NPs as well as for all nanoparticles sizes except for that of [6A], cells can survive internalization and the cell growth process is maintained up

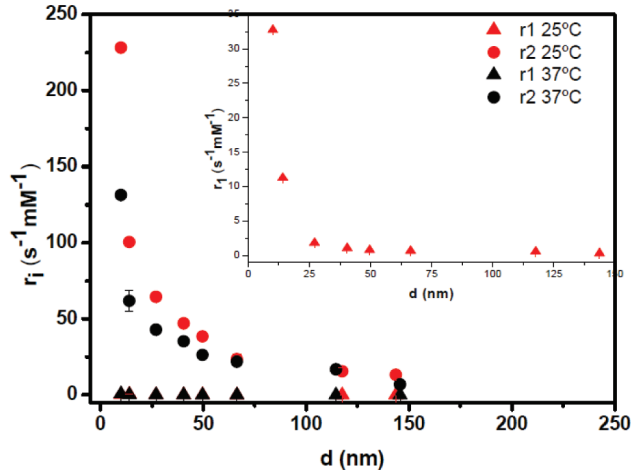


**Figure 4. Dependence of water relaxivities of aqueous suspensions of the γ-$Fe_2O_3$@$SiO_2$ nanoparticles on their diameter, as a result of increased silica layer thickness: (a) inset: $r_1$ at 20 MHz (25 °C); (b) main plot: $r_i$ ($i$ = 1, 2) at 500 MHz (25 and 37 °C). $r_2$ relaxivities were measured at $\tau_{CP}$ = 1.6 ms.**

to 144 h. Additionally, cells internalized with both γ-$Fe_2O_3$ or γ-$Fe_2O_3$@$SiO_2$ particles exhibit the same lag phase of 48 h as the control ones.

The MTT test characteristic of the mitochondrial dehydrogenase activity was performed after NPs cell internalization. This metabolic test is illustrated in Figure 7 by the measurement of the 570 nm absorbance of incubated cells at different time course with different sizes of core−shell NPs.

Both coated and uncoated particles induce an optical density of the cells, which varies with the incubation time reaching a maximum value at 120 h, following the same behavior as the control cells. Like the cell growth in the preceding experiment, the dehydrogenase activity is not affected by NPs internalization in the cells from FF to 4A. In these experiments, the crude analysis of the dehydrogenase activity is relevant for the cell viability, but it is not sufficient to give information about modifications of the cell phenotype. However, the dehydrogenase activity is drastically modified for the larger particles (*e.g.*, 6A). Such nanoparticles are

**TABLE 2. Parameters Obtained from Analysis of $r_2$ ($\tau_{CP}$ = 1.6 ms) and $R_2^*$ Values of Aqueous Suspensions of Core−Shell (γ-$Fe_2O_3$@$SiO_2$) Nanoparticles at $B_0$ = 11.7 T and 25 °C**

| sample | diameter (nm) | $r_2$ ($s^{-1}$ $mM^{-1}$) | $R_2^*$ ($s^{-1}$ $mM^{-1}$) | $2r_i$ (nm) | $2r_{diff}$ (nm) |
|---|---|---|---|---|---|
| FF (core) | 10 ± 2 | 228 ± 2 | 230 ± 1 | 13 ± 1 | 13 ± 1 |
| 0A | 14 ± 2 | 100 ± 1 | 103 ± 1 | 29 ± 1 | 30 ± 1 |
| 1A | 27 ± 5 | 64 ± 2 | 68 ± 1 | 44 ± 1 | 46 ± 2 |
| 2A | 40 ± 8 | 47 ± 2 | 58 ± 1 | 52 ± 1 | 63 ± 3 |
| 3A | 50 ± 7 | 38 ± 2 | 57 ± 1 | 53 ± 1 | 77 ± 5 |
| 4A | 66 ± 8 | 23 ± 3 | 52 ± 1 | 58 ± 2 | 126 ± 18 |
| 5A | 114 ± 14 | 15 ± 2 | 35 ± 1 | 86 ± 2 | 192 ± 30 |
| 6A | 145 ± 10 | 13 ± 2 | 33 ± 1 | 90 ± 2 | 225 ± 33 |

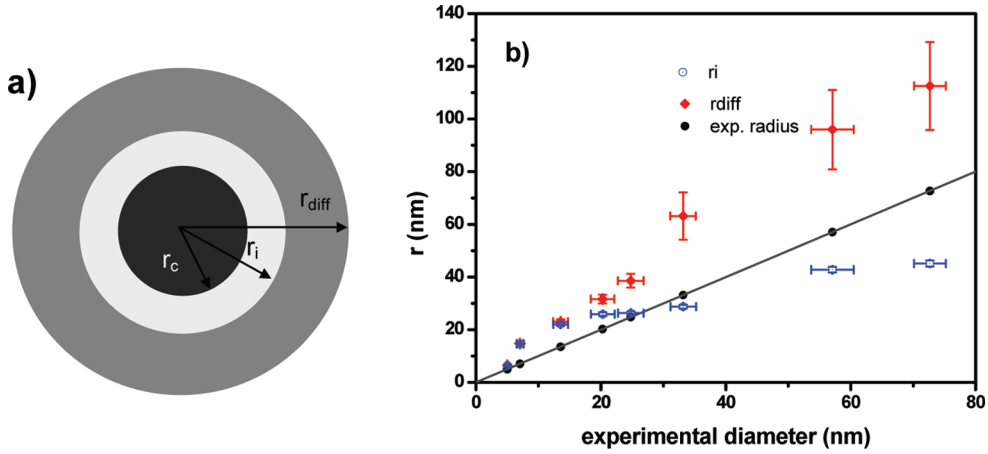


**Figure 5. a) Schematic representation of a γ-$Fe_2O_3$@$SiO_2$ nanoparticle. Here, $r_c$ is the radius of the core and $r_i$ and $r_{diff}$ are the radii of imaginary spheres, as defined in the text. (b) Variation of the silica permeability to water molecules with the shell thickness.**

known to be internalized and stored in lysosome-like vesicles. In the case of NPs 6A, the consequences of their accumulation inside such cells able to phagocytose particles larger than 100 nm are still unknown. Their impact on the local changes in the overall redox potential due to the high load of iron in the vesicles is still an open question. We also normalized the activity per cell as a function of the optical density per million cells as shown in Figure 7b. This allows throughout the duration of the cell culture, the characterization of the cell growth on the dehydrogenase expression and the possible contribution of the NPs uptake during the growth time. The growth of control cells shows a basal level decreasing until 24 h in correlation with the lag phase of growth. Subsequently the expression of the dehydrogenase per cell increases in two major steps, the first one between 48 and 72 h, and the second one between 96 and 144 h. After this period of time, the cells are nearly confluent. When the cells are incubated with NPs, the activity per cell is not significantly affected except for sample 6A after 144 h of exposure. Therefore, one can safely assume that in these conditions, the dehydrogenase expression does not appear to be sensitive to the vesicular load with these core−shell nanoparticles.

## CONCLUSIONS

The understanding of the relationship between the coating properties and the changes in relaxivity is vital for designing magnetic nanoparticle probes for MRI. This is important for medical applications, as higher contrast typically leads to a higher sensitivity and reduces the amount of contrast agent required for imaging. Our choice of a silica coating was motivated by the

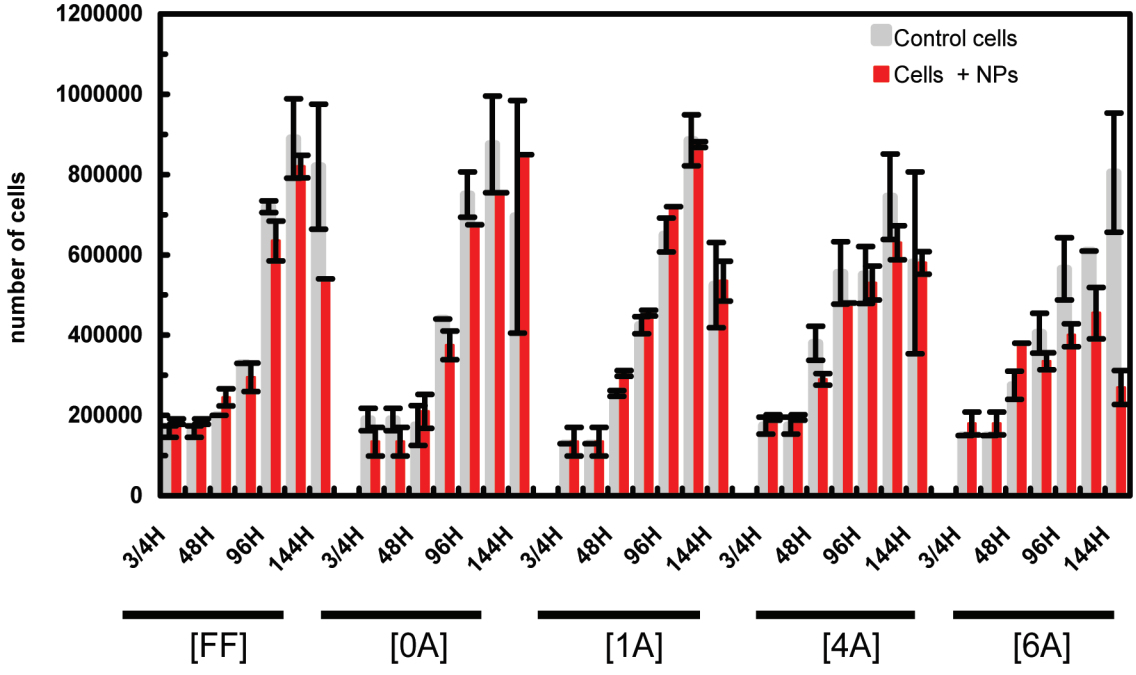


**Figure 6. Cell viability after exposure to different core−shell NPs sizes incubated at different times.**

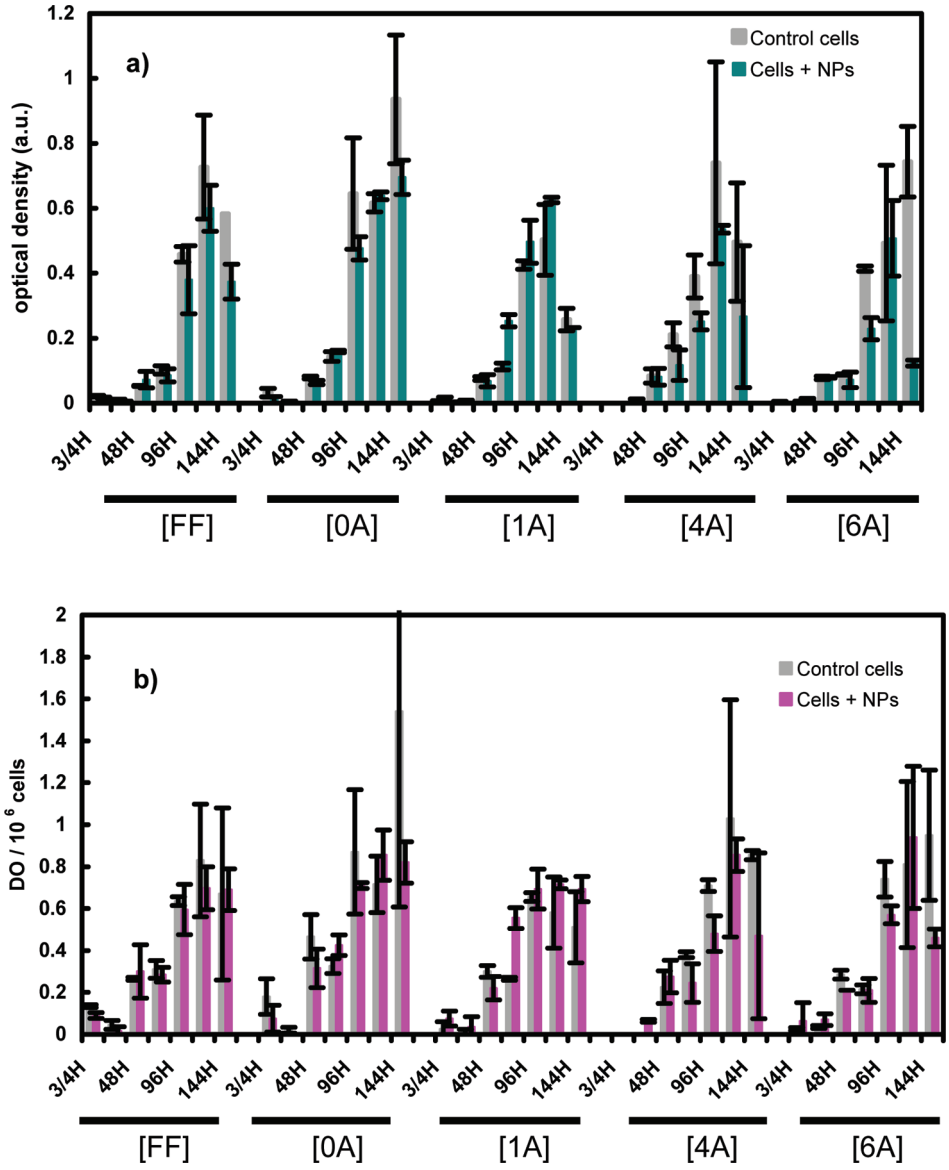


**Figure 7. (a) Variation of total activity and (b) activity per million of cells of mitochondrial dehydrogenase of microglial cells as given by the variation of the solubilized formazan optical density of the medium with incubation times for different sizes of NPs after incubation without (control cells) and with both coated and uncoated particles of different sizes (cells + NPs).**

increased stability of the resulting nanoparticle suspensions and the ensuing ease of conjugation of targeting molecules to the surface of the contrast agents for sensing and imaging. We have shown that in $\gamma$-$Fe_2O_3$@$SiO_2$ core−shell NPs, the coating thickness has a significant impact on their $r_2$ and $r_2^*$ relaxivities at medium and high fields and on $r_1$ relaxivities at medium fields, as a result of decreased outer-sphere relaxation effects. Comparing the $r_2$ and $r_2^*$ values for the different sizes of particles, we were able to identify two types of region in the silica coating, one impermeable close to the $\gamma$-$Fe_2O_3$ core and one permeable to water and at the interface with the bulk water. We have shown that by controlling this coating we are able to tune the size of these two regions. The impermeable region seems to increase only up to a maximum value of 40 nm, while the permeable region goes on increasing with the coating thickness. The diffusion of the water molecules in the permeable silica region is relatively slow resulting in zero contribution to $r_2$. The effect of silica coating of increasing thickness on the $r_2/r_1$ ratio is different from that reported for nanocrystalline superparamagnetic iron oxide NPs (MIONs) coated with a polyethylene glycol (PEG)-modified, phospholipid micelle coating with increasing molecular weights which increase the particle diameter, where this increase causes a $r_2$ decrease and a $r_1$ increase[74]

Therefore, our results provide clues for the design of magnetic-nanoparticle-based contrast agents and their optimization for specific applications in medical diagnosis. This is up to now the only technique to provide clear evidence that a silica layer used as a coating in a core−shell system exhibits regions that are porous to water and other regions that are not.

Careful studies of all the factors that influence the relaxation properties of such contrast agents are under way. The knowledge of theses systems may be extended to other systems and applications. Additionally, preliminary cytotoxicity studies confirmed that these contrast agents do not appear detrimental to microglial cells. However, as the naked nanoparticles have the highest relaxivities, and the coating thickness does not play a role in their cytotoxicity, a preliminary conclusion is that overall optimal particles should have a minimal coating thickness to provide solution stability and a basis for surface conjugation without compromising their relaxivities.

## EXPERIMENTAL DETAILS

**Materials and Purification Methods.** Iron(III) chloride hexahydrate (98%), iron(II) chloride tetrahydrate (99%), iron(III) nitrate nonahydrate (99%), tetraethoxysilane (TEOS) (98%), and citric acid (99.5%) were purchased from Aldrich. Absolute ethanol (J.T. Baker) and ammonia (Carlo Erba) were used as received. All other reagents were of analytical grade.

All the experiments were performed in deionized Milli-Q water.

**Preparation of the Maghemite Ferrofluid Suspension.** The aqueous maghemite suspension was synthesized by precipitation from iron chlorides.[78,79] Briefly, the $Fe_3O_4$ precipitate (black dispersion of magnetite), obtained by alkalinization of the $FeCl_2$ and $FeCl_3$ ($Fe^{2+}/Fe^{3+} = {}^1/_2$) aqueous mixture, was successively oxidized with 2 M $HNO_3$ and 0.33 M $Fe(NO_3)_3 \cdot 9H_2O$ solutions at 100 °C in order to obtain particles with a $Fe^{2+}/Fe^{3+}$ ratio lower than 0.05. With this oxidation process, magnetite is converted into maghemite. The brown dispersion was peptized in a 2 M $HNO_3$ solution under vigorous stirring in order to create positive surface charges. The acidic precipitate was isolated by magnetic separation, washed with acetone, and dispersed at pH ≈ 2.5 in water with nitric acid. The iron concentration was determined by volumetric titration as well as by ICP measurements and the average particle size, as determined by transmission electron microscopy (TEM), was 10 ± 2 nm (see Supporting Information Figures S1−S4 for further characterizations).

**Preparation of the Maghemite Ferrofluid Core−Shell Suspension.** The selected method was derived from the so-called Stöber process[80] widely used for the synthesis of silica beads with diameters from a few tens to a few hundreds of nanometers.[81] It is based on the hydrolysis/condensation of tetraethoxysilane (TEOS) catalyzed by ammonia in alcoholic media. The surface of γ-$Fe_2O_3$ nanoparticles was activated by acidic treatment: where 7.55 mL of γ-$Fe_2O_3$ colloidal suspension (concentration 74.4 g/L) was dispersed in 40 mL of 0.01 M citric acid. They were isolated by decantation on a magnet. The particles were dispersed in 12 mL of water and peptization was performed by adding 20 μL of ammonia. Then, the alkaline sol of citrated-γ-$Fe_2O_3$ nanoparticles was poured in 1 L of ethanol−water−ammonia solution 75/23.5/1.5 v/v/v %, to obtain a 0.561 g/L concentration. The appropriate amounts of TEOS precursors were added to the dispersion under mild stirring to reach the targeted shell thickness. They were added in multiple steps and adjusted in order to reach the desired thickness of the silica shell according to

$$V_{TEOS} = N_{part}[(\rho_{SiO_2} M_{TEOS})/(M_{SiO_2}\rho_{TEOS})]\left[\frac{4}{3}\pi((r + e_{shell})^3 - r^3)\right] \quad (7)$$

where $e_{shell}$ is the shell thickness (the difference $[{}^4/_3\pi(r + e_{shell})^3 - {}^4/_3\pi r^3]$ then corresponding to the volume of the silica shell ($V_{SiO_2}$), $\rho_{SiO_2}$ is the density, and $M_{SiO_2}$ is the molecular weight of $SiO_2$; $V_{TEOS}$, $\rho_{TEOS}$, $M_{TEOS}$ are the volume, density, and molecular weight of TEOS; $N_{part}$ is the number of γ-$Fe_2O_3$ nanoparticles. The very first amount of added TEOS (763 μL) corresponds to the smallest observable silica shell thickness (roughly 1 nm). Then, after 12 h of the reaction, 200 mL of this solution was stocked for analysis and replaced by the same amount of reaction medium. For the following step, the resulting solution was added with the necessary amount of TEOS to increase the shell thickness, and left to react for another 12 h. A 200 mL portion of this solution was also stocked for analysis and replaced by the same amount of reaction medium. This procedure was used repeatedly to increase shell thickness (the number of particles in each volume being recalculated to estimate the right amount of TEOS). Under these conditions, no secondary nucleation was observed, which is in agreement with the results reported by Chen *et al.*[82]

**Particle Characterization.** TEM was performed at room temperature on a JEOL JEM2000 FX transmission electron microscope using an accelerating voltage of 200 kV. Drops of diluted dispersions of core−shell were air-dried on carbon films deposited on 200-mesh copper grids. The excess liquid was blotted with filter paper. The diffuse reflectance infrared Fourier-transform (DRIFT) spectra were recorded on a Bruker IFS Equinox 55FTIR spectrometer (signal averaging 64 scans at a resolution of 4 $cm^{-1}$ in KBr pellets containing *ca.* 2 mass % of material). The zeta potential of the nanoparticles was assessed using a Zetasizer 3000HSA setup (Malvern Instruments) equipped with a He−Ne laser (50 mW, 532 nm). The zeta potential measurement based on laser Doppler interferometry was used to measure the electrophoretic mobility of nanoparticles. Measurements were performed for 20 s using a standard capillary electrophoresis cell. The dielectric constant was set to 80.4 and the Smoluchowsky constant *f*(ka) was 1.5. The iron content was measured by inductively coupled plasma/optical emission spectrometry ICP/OES (ES720, Varian) equipped with a crossflow nebulizer. A 1 g/L iron solution was used to prepare the standard solutions (SCP Science to Paris) and was used as internal standard to evaluate the instrumental drift.

Measurements of water proton longitudinal and transverse relaxation times (T1 and T2, respectively) of aqueous suspensions of the nanoparticles were carried out at 20 MHz on a Bruker Minispec mq20 relaxometer and at 499.83 MHz ($\mathbf{B}_0$ = 11.7 T) on a Varian Unity 500 NMR spectrometer at 25 °C. The T1 relaxation times were measured using the inversion recovery pulse sequence, while the T2 relaxation times were measured using a Carr−PurcellMeiboom−Gill (CPMG) pulse sequence and varying the time interval between two consecutive refocusing pulses ($\tau_{CP}$) in the train of 180° pulses applied. The values of $T_2^*$, the transverse relaxation time in the presence of local field inhomogeneities, were obtained from the water spectral line widths. All the experimental values were corrected for the diamagnetic contribution using aqueous suspensions of hollow silica NPs, to obtain each paramagnetic contribution. These hollow shells where prepared by dilution of the core by addition of concentrated HCl.

**Toxicity Tests.** Cytotoxicity of the γ-$Fe_2O_3$@$SiO_2$ NPs was tested by counting the cells in a Malassez chamber and using the MTT assay to evaluate the cell viability after the nanoparticles preparation process. The core−shell NPs FF, 0A, 1A, 4A, and 6A had diameters ranging between 10 and 143 nm. Briefly, microglial cell lines were seeded at the rate of *ca.* 16 × $10^3$ cells/$cm^2$ in 35 mm diameter plates and allowed to attach for 24 h. The cells were then incubated for 0, 45 min, 24 h, 48 h, 72 h, 96 h, 120 h, and 144 h in 1 mL of culture medium for control cells and supplemented with 60 μL of different NPs (0.16 mM) for treated cells. MTT and counting assays were performed as duplicate for each condition, and the data were averaged. After incubation, cells were scraped from the dishes, then stained with trypan blue and counted with a hemocytometer. The MTT assay is a colorimetric assay that measures the reduction of yellow 3-(4,5-dimethythiazol-2-yl)-2,5-diphenyl tetrazolium bromide (MTT) by dehydrogenase mostly from mitochondria. The MTT enters the cells and passes into the mitochondria, where it is reduced to an insoluble, colored (dark purple) formazan product. After cell culturing in the presence of nanoparticles, 260 μL of the MTT solution in culture medium (0.5 mg/mL) was added into each well. The plate was then incubated at 37 °C in 5% $CO_2$ for 45 min. The medium was removed and 1 mL of PBS solution was added,

then cells were scraped and centrifuged at 1000 rpm for 5 min. The supernatant was removed, 1 mL of dimethyl sulfoxide (DMSO) was added to the pellets to dissolve the formazan crystals, and then it was centrifuged again at 1000 rpm for 5 min. Supernatants were taken and their absorbance was measured with a U-2800A (UV−vis) spectrophotometer (Hitachi, Japan) at 570 nm. Since reduction of MTT can only occur in metabolically active cells, the level of activity is an estimation of the viability of the cells as compared to untreated cells. The cell viability (%) was calculated according to

$$\text{cell viability } \% = \text{OD}_{570}\,(\text{sample})/\text{OD}_{570}\,(\text{control}) \times 100 \quad (8)$$

where $OD_{570}$ (sample) represents the optical density of the wells treated with various iron sizes, and $OD_{570}$ (control) represents that of the wells treated with medium culture.

*Acknowledgment.* This work was supported by the Fundação para a Ciência e Tecnologia (FCT), Portugal (grants to SLCP (SFRH/BD/38313/2007), GAP (SFRH/BPD/35005/2007), and project PTDC/CTM/73243/2006), the CNRS France, the Région Aquitaine France, FEDER, COST Action D38 "Metal-Based systems for Molecular Imaging Applications" and the European Network of Excellence FAME.

*Supporting Information Available:* Synthetic schemes and procedures, characterization of NPs, (XRD, XPS DRIFT and relaxivity measurements. Figure S1: (a) TEM image of $\gamma$-$Fe_2O_3$ nanoparticles used as starting material; (b) histogram with experimental size distribution of the same sample. Figure S2: XRD pattern of the as-synthesized pristine $\gamma$-$Fe_2O_3$. Figure S3: high-resolution XPS spectrum of the Fe2p region of $\gamma$-$Fe_2O_3$. Figure S4: histogram (a) in number; (b) in number, volume, and intensity of $\gamma$-$Fe_2O_3$. Figure S5: synthesis protocol of maghemite core−shell ($\gamma$-$Fe_2O_3$@$SiO_2$) nanoparticles. Figure S6: diffuse reflectance IR Fourier-transform spectra (DRIFT) of (a) maghemite nanoparticles (FF); (b) silica nanoparticles ($SiO_2$); (c) $\gamma$-$Fe_2O_3$@$SiO_2$ (sample 1A). Figure S7: dependence of $r_2$ water proton relaxivities (500 MHz, 25 °C) of aqueous suspensions of the $\gamma$-$Fe_2O_3$@$SiO_2$ nanoparticles on $\tau_{CP}$ as a function of their diameter, as a result of increased silica layer thickness. This material is available free of charge *via* the Internet at http://pubs.acs.org.

## REFERENCES AND NOTES


1. LaConte, L.; Nitin, N.; Bao, G. Magnetic Nanoparticle Probes. *Mater. Today* **2005**, *8*, 3238.
2. Prigogine, I.; Rice, S. A. *Advance in Chemical Physics*; Darmann, J. L., Fiorani, D., Ronc, E., Eds.; Wiley: New York, 1977.
3. Stevens, P. D.; Fan, J.; Gardimalla, H. M. R.; Yen, M.; Gao, Y. Superparamagnetic Nanoparticle-Supported Catalysis of Suzuki Cross-Coupling Reactions. *Org. Lett.* **2005**, *7*, 2085–2088.
4. Mornet, S.; Vasseur, S.; Grasset, F.; Veverka, P.; Goglio, G.; Demourgues, A.; Portier, J.; Pollert, E.; Duguet, E. Magnetic Nanoparticle Design for Medical Applications. *Prog. Solid State Chem.* **2006**, *34*, 237–247.
5. Sieben, S.; Bergemann, C.; Lübe, A.; Brockmann, B.; Rescheleit, D. Comparison of Different Particles and Methods for Magnetic Isolation of Circulating Tumor Cells. *J. Magn. Magn. Mater.* **2001**, *225*, 175–179.
6. Paul, A. L.; Chandra, G. R.; Terstappen, L. W. M. M. Optimization of Ferrofluids and Protocols for the Enrichment of Breast Tumor Cells in Blood. *J. Magn. Magn. Mater.* **2001**, *225*, 301–307.
7. Miller, M. M.; Prinz, G. A.; Cheng, S. F.; Bounnak, S. Detection of a Micron-Sized Magnetic Sphere Using a Ring-Shaped Anisotropic Magnetoresistance-Based Sensor: A Model for a Magnetoresistance-Based Biosensor. *Appl. Phys. Lett.* **2002**, *81*, 2211–2213.
8. Zhao, M.; Josephson, L.; Tang, Y.; Weissleder, R. Magnetic Sensors for Protease Assays. *Angew. Chem., Int. Ed.* **2003**, *42*, 1375–1378.
9. Okuhata, Y. Delivery of Diagnostic Agents for Magnetic Resonance Imaging. *Adv. Drug Delivery Rev.* **1999**, *37*, 121–137.
10. Wunderbaldinger, P.; Josephson, L.; Weissleder, R. Tat Peptide Directs Enhanced Clearance and Hepatic Permeability of Magnetic Nanoparticles. *Bioconjugate Chem.* **2002**, *13*, 264–268.
11. Halavaara, J.; Tervahartiala, P.; Isoniemi, H.; Höckerstedt, K. Efficacy of Sequential Use of Superparamagnetic Iron Oxide and Gadolinium in Liver MR Imaging. *Acta Radiol.* **2002**, *43*, 180–185.
12. Bulte, J. W. Intracellular Endosomal Magnetic Labeling of Cells. *Methods Mol. Med.* **2006**, *124*, 419–439.
13. Modo, M.; Hoehn, M.; Bulte, J. W. Cellular MR Imaging. *Mol. Imaging* **2005**, *4*, 14364.
14. Burtea, C.; Laurent, S.; Roch, A.; Vander Elst, L.; Muller, R. N. C-MALISA (Cellular Magnetic-Linked Immunosorbent Assay), a New Application of Cellular ELISA for MRI. *J. Inorg. Biochem.* **2005**, *99*, 1135–1144.
15. Boutry, S.; Laurent, S.; Vander Elst, L.; Muller, R. N. Specific E-Selectin Targeting with a Superparamagnetic MRI Contrast Agent. *Contrast Med. Mol. Imaging* **2006**, *1*, 15–22.
16. Babes, L.; Denizot, B.; Tanguy, G.; Le Jeune, J. J.; Jallet, P. J. Synthesis of Iron Oxide Nanoparticles Used as MRI Contrast Agents: A Parametric Study. *Colloid Interface Sci.* **1999**, *212*, 474–482.
17. Sonvico, F.; Dubernet, C.; Colombo, P.; Couvreur, P. Metallic Based Nanotechnology, Applications in Diagnosis and Therapeutics. *Curr. Pharm. Des.* **2005**, *11*, 2091–2105.
18. Corot, C.; Robert, P.; Idee, J. M.; Port, M. Recent Advances in Iron Oxide Nanocrystal Technology for Medical Imaging. *Adv. Drug Delivery Rev.* **2006**, *58*, 1471–1504.
19. Jordan, A.; Scholz, R.; Wust, P.; Schirra, H.; Schiestel, T.; Schmidt, H.; Felix, R. Endocytosis of Dextran and Silane-Coated Magnetite Nanoparticles and the Effect of Intracellular Hyperthermia on Human Mammary Carcinoma Cells *in Vitro*. *J. Magn. Magn. Mater.* **1999**, *194*, 185–196.
20. Roullin, V. G.; Deverre, J. R.; Lemaire, L.; Hindré, F.; Julienne, M. C. V.; Vienet, R.; Benoit, J. P. Anti-Cancer Drug Diffusion Within Living Rat Brain Tissue: An Experimental Study Using [3H](6)-5-Fluorouracil-Loaded PLGA Microspheres. *Eur. J. Pharm. Biopharm.* **2002**, *53*, 293–299.
21. Lübbe, A. S.; Alexiou, C. C.; Bergemann, C. Clinical Applications of Magnetic Drug Targeting. *J. Surg. Res.* **2001**, *95*, 200–206.
22. Jain, T. K.; Morales, M. A.; Sahoo, S. K.; Leslie-Pelecky, D. L.; Labhasetwar, V. Iron-Oxide Nanoparticles for Sustained Delivery of Anticancer Agents. *Mol. Pharm.* **2005**, *2*, 194205.
23. Chourpa, L.; Douziech-Eyrolles, L.; Ngaboni-Okassa, L.; Fouquenet, J. F.; Cohen-Jonathan, S.; Souce, M.; Marchais, H.; Dubois, P. Molecular Composition of Iron Oxide Nanoparticles, Precursors for Magnetic Drug Targeting, as Characterized by Confocal Raman Microspectroscopy. *Analyst* **2005**, *130*, 1395–1403.
24. Mary, M. In *Scientific and Clinical Applications of Magnetic Carriers*; Hafeli, U., Schutt, W., Teller, J., Zborowski, M., Eds.; Plenum Press: New York, 1997; pp 303−309.
25. Elaissari, A.; Rodrigue, M.; Meunier, F.; Herve, C. Hydrophilic Magnetic Latex for Nucleic Acid Extraction, Purification and Concentration. *J. Magn. Magn. Mater.* **2001**, *225*, 127–133.
26. Gupta, A. K.; Gupta, M. Synthesis and Surface Engineering of Iron Oxide Nanoparticles for Biomedical Applications. *Biomaterials* **2005**, *26*, 3995–4021.
27. Cornell, R. M., Schwertmann, U., Eds. *The Iron Oxides: Structures, Properties, Reactions, Occurrences and Uses*; Wiley-VCH: Weinheim, Germany, 2003.
28. Josephson, L. Magnetic Nanoparticles for MR Imaging. In *BioMEMS and Biomedical Nanotechnology*; Ferrari, M., Ed.; Springer: New York, 2006; Vol. 1, p 227.

29. Sun, Y. K.; Ma, M.; Zhang, Y.; Gu, N. Synthesis and Characterization of Biocompatible $Fe_3O_4$ Nanoparticles. *Colloids Surf., A* **2004**, *245*, 15–19.
30. Berry, C. C.; Curtis, A. S. G. Functionalisation of Magnetic Nanoparticles for Applications in Biomedicine. *J. Phys. D. Appl. Phys.* **2003**, *36*, R198–R206.
31. Chan, D. C. F.; Kirpotin, D. B.; Bunn, P. A., Jr. Synthesis and Evaluation of Colloidal Magnetic Iron Oxides for the Site-Specific Radio Frequency-Induced Hyperthermia of Cancer. *J. Magn. Magn. Mater.* **1993**, *122*, 374–378.
32. Jana, N. R.; Peng, X. Single-Phase and Gram-Scale Routes toward Nearly Monodisperse Au and Other Noble Metal Nanocrystals. *J. Am. Chem. Soc.* **2003**, *125*, 14280–14281.
33. Sun, S.; Murray, C. B.; Weller, D.; Folks, L.; Moser, A. A. Monodisperse FePt Nanoparticles and Ferromagnetic FePt Nanocrystal Superlattices. *Science* **2000**, *287*, 19891992.
34. Li, J. J.; Wang, Y. A.; Guo, W.; Keay, J. C.; Mishima, T. D.; Johnson, M. B.; Peng, X. Large-Scale Synthesis of Nearly Monodisperse CdSe/CdS Core/Shell Nanocrystals Using Air-Stable Reagents *via* Successive Ion Layer Adsorption and Reaction. *J. Am. Chem. Soc.* **2003**, *125*, 12567–12575.
35. Murray, C. B.; Norris, D. J.; Bawendi, M. G. Synthesis and Characterization of Nearly Monodisperse CdE (E = S, Se, Te) Semiconductor Nanocrystallites. *J. Am. Chem. Soc.* **1993**, *115*, 8706–8715.
36. Sun, S.; Zeng, H. Monodisperse $Mfe_2O_4$ (M = Fe, Co, Mn) Nanoparticle. *J. Am. Chem. Soc.* **2002**, *124*, 8204–8205.
37. Jana, N. R.; Chen, Y.; Peng, X. Size- and Shape-Controlled Magnetic (Cr, Mn, Fe, Co, Ni) Oxide Nanocrystals *via* a Simple and General Approach. *Chem. Mater.* **2004**, *16*, 39313935.
38. Hyeon, T.; Lee, S. S.; Park, J.; Chung, Y.; Na, H. B. Synthesis of Highly Crystalline and Monodisperse Maghemite Nanocrystallites without a Size-Selection Process. *J. Am. Chem. Soc.* **2001**, *123*, 12798–12801.
39. Wu, W.; He, Q.; Jiang, C. Magnetic Iron Oxide Nanoparticles: Synthesis and Surface Functionalization Strategies. *Nanoscale Res. Lett.* **2008**, *3*, 397–415.
40. Gao, X.; Cui, Y.; Levenson, R. M.; Chung, L. W. K.; Nie, S. *In Vivo* Cancer Targeting and Imaging with Semiconductor Quantum Dots. *Nat. Biotechnol.* **2004**, *22*, 969–976.
41. Pellegrino, T.; Manna, L.; Kudera, S.; Liedl, T.; Koktysh, D.; Rogach, A. L.; Keller, S.; Radler, J.; Natile, G.; Parak, W. Hydrophobic Nanocrystals Coated with an Amphiphilic Polymer Shell: A General Route to Water Soluble Nanocrystals. *Nano Lett.* **2004**, *4*, 703–707.
42. Guo, W.; Li, J. J.; Wang, Y. A.; Peng, X. Luminescent CdSe/CdS Core/Shell Nanocrystals in Dendron Boxes: Superior Chemical, Photochemical, and Thermal Stability. *J. Am. Chem. Soc.* **2003**, *125*, 3901–3909.
43. Kim, M.; Chen, Y.; Liu, Y.; Peng, X. Super-stable, High-quality $Fe_3O_4$ Dendron-Nanocrystals Dispersible in Both Organic and Aqueous Solutions. *Adv. Mater.* **2005**, *17*, 14291436.
44. Kim, S. W.; Kim, S.; Tracy, J. B.; Jasanoff, A.; Bawendi, M. G. Phosphine Oxide Polymer for Water-Soluble Nanoparticles. *J. Am. Chem. Soc.* **2005**, *127*, 4556–4557.
45. Schroedter, A.; Weller, W. Ligand Design and Bioconjugation of Colloidal Gold Nanoparticles. *Angew. Chem., Int. Ed.* **2002**, *41*, 3218–3221.
46. Lee, D. C.; Mikulec, F. V.; Pelaez, J. M.; Koo, B.; Korgel, B. A. Synthesis and Magnetic Properties of Colloidal $MnPt_3$ Nanocrystals. *J. Phys. Chem. B* **2006**, *110*, 11160.
47. Veiseh, O.; Sun, C.; Gunn, J.; Kohler, N.; Gabikian, P.; Lee, D.; Bhattarai, N.; Ellenbogen, R.; Sze, R.; Hallahan, A.; Olson, J.; *et al.* An Optical and MRI Multifunctional Nanoprobe for Targeting Gliomas. *Nano Lett.* **2005**, *5*, 1003–1008.
48. Liu, X.; Xing, J.; Guan, Y.; Shan, G.; Liu, H. Synthesis of Amino-Silane Modified Superparamagnetic Silica Supports and Their Use for Protein Immobilization. *Colloids Surf. A* **2004**, *238*, 127–131.
49. Yi, D. K.; Selvan, S. T.; Lee, S. S.; Papaefthymiou, G. C.; Kundaliya, D.; Ying, J. Y. Silica-Coated Nanocomposites of Magnetic Nanoparticles and Quantum Dots. *J. Am. Chem. Soc.* **2005**, *127*, 4990–4991.
50. Schroedter, A.; Weller, W.; Eritja, R.; Ford, W. E.; Wessels, J. M. Biofunctionalization of Silica-Coated CdTe and Gold Nanocrystals. *Nano Lett.* **2002**, *2*, 1363–1367.
51. Bruchez, M.; Moronne, M.; Gin, P.; Weiss, S.; Alivisatos, A. P. Semiconductor Nanocrystals as Fluorescent Biological Labels. *Science* **1998**, *281*, 2013–2016.
52. Gerion, D.; Pinaud, F.; Williams, S. C.; Parak, W. J.; Zanchet, D.; Weiss, S.; Alivisatos, A. P. Synthesis and Properties of Biocompatible Water-Soluble Silica-Coated CdSe/ZnS Semiconductor Quantum Dots. *J. Phys. Chem. B* **2001**, *105*, 8861–8871.
53. Darbandi, M.; Thomann, R.; Nann, T. Single Quantum Dots in Silica Spheres by Microemulsion Synthesis. *Chem. Mater.* **2005**, *17*, 5720–5725.
54. Sousa, M. H.; Rubim, J. C.; Sobrinho, P. G.; Tourinho, F. A. Biocompatible Magnetic Fluid Precursors Based on Aspartic and Glutamic Acid Modified Maghemite Nanostructures. *J. Magn. Magn. Mater.* **2001**, *225*, 67–72.
55. Mornet, S.; Vasseur, S.; Grasset, F.; Duguet, E. Magnetic Nanoparticles Design for Medical Diagnosis and Therapy. *J. Mater. Chem.* **2004**, *14*, 2161–2175.
56. Xie, J.; Wang, C. H. Self-Assembled Biodegradable Nanoparticles Developed by Direct Dialysis for the Delivery of Paclitaxel. *Pharm. Res.* **2005**, *22*, 2079–2090.
57. He, H.; Liu, H.; Zhou, K.; Wang, W.; Rong, P. Characteristics of Magnetic $Fe_3O_4$ Nanoparticles Encapsulated with Human Serum Albumin. *J. Cent. South Univ. Technol.* **2006**, *13*, 6–11.
58. Tiefenauer, L. X.; Kuhne, G.; Andres, R. Y. Antibody-Magnetite Nanoparticles: *In Vitro* Characterization of a Potential Tumor-Specific Contrast Agent for Magnetic Resonance Imaging. *Bioconjugate Chem.* **1993**, *4*, 347352;.
59. Nam, J. M.; Stoeva, S. I.; Mirkin, C. A. Bio-Bar-Code-Based DNA Detection with PCR-like Sensitivity. *J. Am. Chem. Soc.* **2004**, *126*, 5932–5933.
60. Lewin, M.; Carlesso, N.; Tung, C.-H.; Tang, X.-W.; Cory, D.; Scadden, D. T.; Weissleder, R. Tat Peptide-Derivatized Magnetic Nanoparticles Allow *In Vivo* Tracking and Recovery of Progenitor Cells. *Nat. Biotechnol.* **2000**, *18*, 410–414.
61. Weizmann, Y.; Patolsky, F.; Lioubashevski, O.; Willner, I. Magneto-mechanical Detection of Nucleic Acids and Telomerase Activity in Cancer Cells. *J. Am. Chem. Soc.* **2004**, *126*, 1073–1080.
62. Lartigue, L.; Oumzil, K.; Guari, Y.; Larionova, J.; Guérin, C.; Montero, J. L.; Barragan-Montero, V.; Sangregorio, C.; Caneschi, A.; Innocenti, C.; Kalaivani, T.; *et al.* Water-Soluble Rhamnose-Coated $Fe_3O_4$ Nanoparticles. *Org. Lett.* **2009**, *11*, 2992–2995.
63. Ashtari, P.; He, X.; Wang, K.; Gong, P. An Efficient Method for Recovery of Target ssDNA Based on Amino-Modified Silica-Coated Magnetic Nanoparticles. *Talanta* **2005**, *67*, 548–554.
64. Allemann, E.; Gurny, R.; Doelker, E. Drug Loaded Nanoparticles—Preparation Methods and *In Vivo* Studies. *Eur. J. Pharm. Biopharm.* **1993**, *39*, 173–191.
65. Lu, Y.; Yin, Y.; Mayers, B. T.; Xia, Y. Synthesis and Self-Assembly of Au@$SiO_2$ Core−Shell Colloids. *Nano Lett.* **2002**, *2*, 183–186.
66. Mornet, S.; Elissalde, C.; Hornebeck, V.; Bidault, O.; Duguet, E.; Brisson, A.; Maglione, M. Controlled Growth of Silica Shell on $Ba_{0.6}Sr_{0.4}TiO_3$ Nanoparticles Used as Precursors of Ferroelectric Composites. *Chem. Mater.* **2005**, *17*, 4530.
67. Gaudon, M.; Basly, B.; Fauque, Y.; Majimel, J.; Delville, M. H. Thermochromic Phase Transition on $CuMo_{0.9}W_{0.1}O_4$@$SiO_2$ Core−Shell Particles. *Inorg. Chem.* **2009**, *48*, 21362139.
68. Muller, R. N.; Roch, A.; Colet, J.-M. ; Ouakssim, A.; Gillis, P. Particulate Magnetic Contrast Agents. In *The Chemistry of Contrast Agents in Medical Magnetic Resonance Imaging*; Merbach, A. E., Tóth, É., Eds.: Wiley: New York, 2001; Chapter 10, pp 417−435.
69. Laurent, S.; Forge, D.; Port, M.; Roch, A.; Robic, C.; Vander Elst, L.; Muller, R. N. Magnetic Iron Oxide Nanoparticles: Synthesis, Stabilization, Vectorization, Physicochemical

Characterizations, and Biological Applications. *Chem. Rev.* **2008**, *108*, 2064–2110.
70. Gueron, M. Nuclear Relaxation in Macromolecules by Paramagnetic Ions. Novel Mechanism. *J. Magn. Reson.* **1975**, *19*, 58–66.
71. Roch, A.; Muller, R. N. Longitudinal Relaxation of Water Protons in Colloidal Suspensions of Superparamagnetic Crystals. *Proc. 11th Annu. Meet. Soc. Magn. Reson. Med.* **1992**, *11*, 1447.
72. Roch, A.; Muller, R. N.; Gillis, P. Theory of Proton Relaxation Induced by Superparamagnetic Particles. *J. Chem. Phys.* **1999**, *110*, 5403–5411.
73. Gillis, P.; Moiny, F.; Brooks, R. A. On T-2-Shortening by Strongly Magnetized Spheres: A Partial Refocusing Model. *Magn. Reson. Med.* **2002**, *47*, 257–263.
74. LaConte, L. E. W.; Nitin, N.; Kurkiya, O.; Caruntu, D.; O'Connor, C. J.; Hu, X.; Bao, G. Coating Thickness of Magnetic Iron Oxide Nanoparticles Affects *R*2 Relaxivity. *J. Magn. Res. Imaging* **2007**, *26*, 1634–1641.
75. Norek, M.; Pereira, G. A.; Geraldes, C. F. G. C.; Denkova, A.; Zhou, W.; Peters, J. A. NMR Transversal Relaxivity of Suspensions of Lanthanide Oxide Nanoparticles. *J. Phys. Chem. C* **2007**, *111*, 10240–10246.
76. Pereira, G. A.; Norek, M.; Peters, J. A.; Ananias, D.; Rocha, J.; Geraldes, C. F. G. C. NMR Transversal Relaxivity of Aqueous Suspensions of Particles of $Ln^{3+}$-Based Zeolite Type Materials. *Dalton Trans* **2008**, 2241–2247; DOI: 10.1039/b718438g.
77. Voisin, P.; Ribot, E. J.; Miraux, S.; Bouzier-Sore, A.-K.; Lahitte, J.-F.; Bouchaud, V.; Mornet, S.; Thiaudière, E.; Franconi, J.-M.; Delville, M.-H. Use of Lanthanide-Grafted Inorganic Nanoparticles as Effective Contrast Agents for Cellular Uptake Imaging. *Bioconjugate Chem.* **2007**, *18*, 1053–1063.
78. Massart, R. Preparation of Aqueous Ferrofluids without Using Surfactant; Behavior as a Function of pH and Counterions. *C.R. Acad. Sci.* **1980**, *291*, C1.
79. Mornet, S.; Grasset, F.; Portier, J.; Duguet, E. Maghemite@Silica Nanoparticles for Biological Applications. *Eur. Cells Mater.* **2002**, *3*, 110–113.
80. Stöber, W.; Fink, A.; Bohn, E. Controlled Growth of Monodisperse Silica Spheres in the Micron Size Range. *J. Colloid Interface Sci.* **1968**, *26*, 62.
81. Nozawa, K.; Gailhanou, H.; Raison, L.; Panizza, P.; Ushiki, H.; Sellier, E.; Delville, J. P.; Delville, M. H. Smart Control of Monodisperse Stöber Silica Particles: Effect of Reactant Addition Rate on Growth Process. *Langmuir* **2005**, *21*, 1516–1523.
82. Chen, S.-L.; Dong, P.; Yang, G.-H.; Yang, J. J. Characteristic Aspects of Formation of New Particles during the Growth of Monosize Silica Seeds. *J. Colloid Interface Sci.* **1996**, *180*, 237–241.